Phase diagram of the quantum Ising model with long-range interactions on an infinite-cylinder triangular lattice

S. N. Saadatmand,[1,2,*] S. D. Bartlett,[3] and I. P. McCulloch[2]

[1]*Centre for Quantum Computation and Communication Technology (Australian Research Council), Centre for Quantum Dynamics, Griffith University, Brisbane, Queensland 4111, Australia*

[2]*ARC Centre of Excellence for Engineered Quantum Systems, School of Mathematics and Physics, The University of Queensland, St Lucia, QLD 4072, Australia*

[3]*ARC Centre of Excellence for Engineered Quantum Systems, School of Physics, The University of Sydney, Sydney, NSW 2006, Australia*

(Received 13 February 2018; revised manuscript received 28 March 2018; published 9 April 2018)

Obtaining quantitative ground-state behavior for geometrically-frustrated quantum magnets with long-range interactions is challenging for numerical methods. Here, we demonstrate that the ground states of these systems on two-dimensional lattices can be efficiently obtained using state-of-the-art translation-invariant variants of matrix product states and density-matrix renormalization-group algorithms. We use these methods to calculate the fully-quantitative ground-state phase diagram of the long-range interacting triangular Ising model with a transverse field on six-leg infinite-length cylinders and scrutinize the properties of the detected phases. We compare these results with those of the corresponding nearest neighbor model. Our results suggest that, for such long-range Hamiltonians, the long-range quantum fluctuations always lead to long-range correlations, where correlators exhibit power-law decays instead of the conventional exponential drops observed for short-range correlated gapped phases. Our results are relevant for comparisons with recent ion-trap quantum simulator experiments that demonstrate highly-controllable long-range spin couplings for several hundred ions.

DOI: 10.1103/PhysRevB.97.155116

I. INTRODUCTION

The zero-temperature physics of geometrically-frustrated magnets with short-range (SR) interactions, i.e., interactions decaying exponentially with distance, is relatively well understood [1–6]. A frustration-free spin system with dominant antiferromagnetic (AFM) local couplings commonly exhibit a bipartite Néel-type [7] ground state, while in Heisenberg-type models, frustration can lead to the stabilization of a variety of exotic forms of the quantum matter such as spin glasses [2,4,5], topological [8–10] and algebraic [8] spin liquids, and many-sublattice long-range order [1–6]. In contrast, little is known about the properties of long-range (LR) interacting spin systems, with or without frustration, in particular for lattice dimension greater than one. (For results on LR-interacting AFM Heisenberg-type chains, see Refs. [11–16] and also below.) In this context, LR refers to interactions decaying as $1/r^{\alpha}$, where r denotes the real-space distance between two sites measured in units of the lattice spacing. For example, $\alpha = 2$ corresponds to natural monopole-dipole-type interactions, and $\alpha = 3$ to dipole-dipole-type atomic couplings. We do not yet have a complete theory that would govern the physics of such LR-interacting Hamiltonians in two dimensions. In particular, consider the LR-interacting triangular quantum Ising model (defined in details below). Due to its two-dimensional arrangement, high degree of geometrical frustration, and the long-range nature of the couplings, the ground state properties of this system are not yet fully understood.

Recently, the LR-interacting triangular quantum Ising model has been simulated *experimentally* with ions confined in a Penning trap [17,18] (see also Refs. [19,20]). These experiments simulate LR interactions of hundreds of spins on a two-dimensional lattice, and it is believed that classical numerical simulations for generic LR Hamiltonians on systems of this size will be intractable. This perceived classical intractability is a principal motivation for the development of "quantum simulations" [21,22]. Experiments that implement quantum simulations can efficiently access the physics of quantum many-body systems, whereas exact classical simulations would have a complexity that scales exponentially with the number of spins. (See Refs. [23,24] for reviews and critical discussions of engineered quantum simulators.)

In this paper, we demonstrate that modern well-controlled approximate numerical methods can be used to probe this regime. Specifically, we establish that state-of-the-art variants of translation-invariant matrix product states (MPS) [25–31] and density-matrix renormalization-group (DMRG) [27,28,30,32,33] can be used to find the detailed phase diagram of the LR-interacting triangular quantum Ising Hamiltonian on infinite cylinders. These results constitute an important first step in assessing whether or not the physics of LR-interacting quantum many-body systems, now accessible through quantum simulator experiments [17–19], can also be accessed through classical numerical simulation methods. Our results give strong evidence that they can be. Furthermore, we note that our results of the LR-interacting triangular quantum Ising model on cylinders are (to the best of our knowledge) the first attempt to create an infinite-size MPS/DMRG phase diagram of any two-dimensional LR-interacting model.

*n.saadatmand@griffith.edu.au

A. Characteristics of LR-interacting quantum magnets

Long-range interacting spin systems exhibit some peculiar characteristics in comparison to their short-range interacting counterparts. Most strikingly, the presence of long-range interactions can break continuous symmetries in low dimensions [34], which is strictly forbidden for SR-interacting Hamiltonians due to the Mermin-Wigner-Hohenberg theorem [35,36]. Examples of symmetry breaking due to long-range interactions include the XXZ chain exhibiting $U(1)$ symmetry breaking at zero temperatures [34] and the square-lattice XXZ model exhibiting $U(1)$ symmetry breaking at finite temperatures [37].

Furthermore, while SR-correlated gapped phases in low dimensions collectively obey an area law for the entanglement entropy [38–41], Koffel *et al.* [42] suggests the existence of sublogarithmic corrections to, or the breakdown of, the area law in LR-correlated states for $\alpha < 2$. Gong *et al.* [43] has recently established that, for arbitrary-dimension LR-interacting systems, a 'dynamical' variant of the area law holds for $\alpha > \mathrm{Dim} + 1$, considering the rate of entanglement entropy growth of time-evolved states (see also Ref. [44]), and $\alpha > 2(\mathrm{Dim} + 1)$, considering the entanglement entropy of the ground states of an effective Hamiltonian.

For the purpose of the current study, the most relevant distinction between SR and LR interactions emerges from the realization [45] that, for the LR-interacting transverse-field Ising chain, the paramagnet and Z_2-symmetry-broken AFM ground states exhibit a bulk spin gap (spin-flop excitations) and, although the correlations drop exponentially for short distances, the decay is algebraic (power-law) for long distances. We contrast this behavior with the nearest neighbor Ising model, which exhibits short-range correlated paramagnetic and AFM ground states and where power-law correlations occur only at the second-order transition in between these two phases. Moreover, in the square-lattice XXZ model with dipole-dipole LR interactions, the Ising-type AFM ground state also exhibits power-law-decaying correlation functions [37]. Such power-law decays are distinct from the exponential-decaying area-law-obeying correlations observed in SR-correlated phases.

B. Details of the LR Ising Hamiltonian

The specific Hamiltonian that will be the focus of our investigation is the antiferromagnetic LR-interacting triangular quantum Ising model (LR-TQIM) with a transverse field. It can be written as

$$H_{\mathrm{LR}} = J \sum_{i>j} \frac{1}{r_{ij}^{\alpha}} S_i^z S_j^z + \Gamma \sum_i S_i^x, \tag{1}$$

where i and j specify physical sites on vertices of the triangular lattice, r_{ij} denotes the real-space (chord) distance between site i and j, and we set $J = 1$ as the unit of energy. For $\alpha \to \infty$, H_{LR} reduces to the nearest neighbor model (NN-TQIM),

$$H_{NN} = \sum_{\langle i,j \rangle} S_i^z S_j^z + \Gamma \sum_i S_i^x, \tag{2}$$

where $\langle i,j \rangle$ stands for summing over only NN spins. The low-temperature properties of this NN model are generally well understood (see Refs. [46–50] and also below).

The experiments by Britton *et al.* [17] and Bohnet *et al.* [18] engineered a variable-range many-body model of hundreds of LR-interacting spin-$\frac{1}{2}$ $^9Be^+$ ions on a triangular lattice, using a disk-shaped Penning trap with single-spin readout capability. These experiments established that it is practical to construct the Hamiltonian of Eq. (1) for hundreds of spins, in the regime of $0 \leqslant \alpha \leqslant 3.0$. For such a finite set of spins and vanishing Γ (the classical model), Britton *et al.* [17] observed power-law decay of spin correlations for a variety of α values. Moreover, they verified the existence of a power-law-decaying AFM ground state for $0.05 \lesssim \alpha \lesssim 1.4$ using a mean-field theory approach.

Many possibilities for further research are opened up by these experiments, such as the possibility of experimental simulations of spin dynamics in two dimensions and effects of disorder and many-body localization, e.g., see Ref. [51]. Although energy scaling arguments [52] suggest that many-body localization does *not* occur in Dim > 1, at least in the thermodynamic limit, signatures of localization have been observed in two-dimensional disordered optical lattices [53]. Localization has also been observed in small ion trap systems of up to 10 long-range interacting spins [54,55]. Penning traps offer an order of magnitude increase in the number of spins, which makes them an ideal setup for simulating two-dimensional physics.

C. Existing results on the nature of LR-TQIM

Previous analytical and numerical works on LR-TQIM and its NN limit have provided some preliminary understanding of the physics. For the classical NN model (i.e., $\alpha \to \infty$, as in Eq. (2), and in the absence of the field, $\Gamma = 0$), thermodynamic-limit historical studies exist: The lowest-energy state is a highly (macroscopic) degenerate finite-entropy phase at all finite temperatures [56]; this phase exhibits *no* long-range order, $T = 0$ being the Néel critical point [57], while the ground state exhibits critical $\langle S_0^z S_r^z \rangle$ correlations decaying oscillatory as $\frac{1}{r^{1/2}}$. For finite values of the field in Eq. (2), using quantum-to-classical Suzuki mapping [58], we note that NN-TQIM corresponds to a finite-temperature classical ferromagnetically stacked layers of triangular AFM Ising planes (effectively replacing Γ with the temperature for the classical 3D model). The latter system also has as macroscopically degenerate ground state (however, without the finite entropy). Interestingly, it undergoes the classical version of the "order from disorder" phenomenon [50,59,60] (induced by thermal fluctuations), which chooses an ordered state with the expected wave vector of $Q_{\text{finite-T}}^{\text{classical}} = (\pm\frac{2\pi}{\sqrt{3}}, \pm\frac{2\pi}{3})$ in our notation (i.e., the family of three-sublattice orders that form a regular-hexagonal-shaped first Brillouin zone—see below for our notation of lattice vectors). Consistent with this, for $\Gamma \lesssim 0.705$ (using our Hamiltonian conventions), Penson *et al.* [50] observed the same $Q_{\text{finite-T}}^{\text{classical}}$-ordered ground state for H_{NN} with power-law-decaying correlations; above the $\Gamma_c \approx 0.705$ critical point, the authors argue for another power-law-decaying ground state with a different exponent, a finite bulk gap, and no degeneracy (we expect this to be the partially x-polarized FM phase as found below). Subsequently, quantum Monte Carlo (QMC) calculations [46,48] verified the stabilization of a three-sublattice AFM ordered ground

state for the weak fields. Importantly, these authors noted that the small-Γ NN-TQIM can be also mapped to a quantum dimer model ($\frac{v}{t} \to 0$ limit of Rokhsar-Kivelson Hamiltonian, H_{QDM}) on a dual kagomé lattice formed by the centers of the triangular plaquettes. Such dimer arrangements can be labeled using the so-called 'height configurations' [46,47]. In fact, the existence of the map to the height model already means that the classical model should exhibit power-law correlations [46] under a set of 'reasonable' assumptions. H_{QDM}, which corresponds to the NN-TQIM, exhibits a series of uniform ground states with valence-bond solid ordering that translates to three-sublattice orders on the triangular lattice (will be stated as (S^z_a, S^z_b, S^z_c), whereby $S^z_{\{a,b,c\}}$ stands for local spin polarization in spins' z direction of vertices $\{a,b,c\}$ for a three-site unit cell formed by a triangular plaquette). Such ordering was previously observed in Landau-Ginzburg-Wilson analyses [59,61] of three-dimensional FM stacked triangular AFM Ising lattices, where it called a 'clock' order due to the appearance of a sixfold clock term breaking the XY symmetry. Let us now summarize the existing results on the phase diagram of NN-TQIM at $T = 0$: Refs. [48,59] found that the model undergoes a quantum phase transition in the universality class of 3D-XY, namely from a clock order in the low fields to a S_z-magnetization-disordered (x-polarized FM) ground state in the large fields (the existence of such a universality class was later advocated for the LR model too by Humeniuk [62]). Furthermore, QMC simulations of Refs. [46,48] suggest the selection of $(0.5, -0.5, 0)$ ordering for the clock phase having zero net magnetization (which corresponds to a 'hierarchical' plaquette order on the dimer model).

In contrast to the NN model, there are few existing studies of the long range model. The most comprehensive is by Humeniuk [62], which presents both thermodynamic-limit mean-field analyses (for a wide range of α) and stochastic-series-expansion QMC simulations (only for $\alpha = 3.0$) of Eq. (1) on disk-shaped, open-boundary-conditioned triangular lattices hosting up to 301 spins for a variety of Γ values. A semiquantitative phase diagram is constructed for the model with the main high-precision QMC results only available at $\alpha = 3.0$ but for a wide range of field values. In this study, it was found that, for large enough α, the clock-ordered phase chooses the sublattice structure of $(0.5, -0.25, -0.25)$, i.e., the so-called 120° order. This result differs from the phase diagram of the NN model from Refs. [46,48] and with our results (see below). While the $(0.5, -0.5, 0)$ ordering for the large-α limit is argued by the present and two other numerical studies, we note that such a difference might be still due to the restricted lattice geometry employed in our calculations and different handling of the QMC's inherent sign problem for the frustrated systems in Refs. [46,48] and Ref. [62]. Nevertheless, the quantitative phase diagram and the realization of three distinct phase regions (including the clock and x-polarized FM ordering) in Ref. [62] is in line with our findings.

D. MPS and DMRG algorithms for LR interactions

Variants of MPS and DMRG algorithms (see Refs. [30,63] for reviews) have already revolutionized our understanding of the low-energy physics of low-dimensional local Hamiltonians by providing an efficient platform for numerical simulations. The success of these algorithms in capturing the properties of such Hamiltonians can be best understood through the MPS description, i.e., the wave-function ansatz that underlies DMRG. However, when one considers LR-interacting models, finite-size numerical approaches suffer from the explicit existence of a cutoff or other ways of limiting the range of LR couplings and, therefore, exhibit strong boundary effects. As such, many of these algorithms may not capture the essential physics associated with LR fluctuations. Later in this paper, we will see some discrepancies between finite-size calculations and our infinite-size results.

However, MPS algorithms that act directly in the thermodynamic limit such as iDMRG [28], which contain fixed-point transfer matrix equations and naturally live in the thermodynamic limit at least in one spatial direction, can be more efficient for LR models such as Eq. (1). The key innovation here was in the realization that MPS can also describe the low-energy sector of Hamiltonians with rapidly (i.e., *exponentially*) decaying interactions [28,64]. Specifically, Refs. [28,64] established that matrix product operators [27,28,30,65] (MPOs), which are MPS-based representations of operators, can be written to include exponential-decaying couplings such as $e^{-\lambda r}$ (see below). Fortunately, this method is sufficient to describe LR decays as well, since one can expand an algebraically decaying function in terms of the sum of some exponential terms. As an example,

$$\frac{1}{r^\alpha} \simeq \sum_{i=1}^{n_{\text{cutoff}}} a_i e^{-\lambda_i r}, \tag{3}$$

where a_i and λ_i are constants to be fitted, for example by using a nonlinear least-square method. Obviously, the expansion is only exact if $n_{\text{cutoff}} \to \infty$. The existence of n_{cutoff} means that we still face a distance scale cutoff, that is, iMPS should only be considered as an improvement over finite-size calculations with a fixed cutoff for the interaction lengths. However, in practice, a small n_{cutoff} can often be chosen for iDMRG simulations in a way that describes the LR physics very well. We can therefore replace a LR Hamiltonian such as H_{LR} with an approximate one, $H_{\text{LR-approx}}$, in the form of

$$\begin{aligned} H_{\text{LR}} \quad &\longleftrightarrow \\ H_{\text{LR-approx}} &= \sum_{i>j} \left(\sum_{k=1}^{n_{\text{cutoff}}} a_k(i,j) e^{-\lambda_k(i,j) r_{ij}} \right) S^z_i S^z_j \\ &\quad + \Gamma \sum_i S^x_i . \end{aligned} \tag{4}$$

Consider a rather simple LR-interacting system: the one-dimensional exactly-solvable Haldane-Shastry model [66,67] $H_{\text{Haldane-Shastry}} = J \sum_{i>j} \frac{1}{r^2_{i,j}} \mathbf{S}_i \cdot \mathbf{S}_j$. This model has known ground state energy per site of $-\frac{\pi}{4}$ in the thermodynamic limit (in the units of J). A quick iDMRG calculation with $n_{\text{cutoff}} = 5$ (not detailed here) reproduces the excellent residual energy per site of $\Delta E = E_{\text{iDMRG}} - E_{\text{exact}} = 1.15(2) \times 10^{-5}$ for just $m_{\text{max}} = 100$, while Ref. [64] kept up to $n_{\text{cutoff}} = 9$ and reproduced an energy per site with the best accuracy of $\Delta E \approx 2 \times 10^{-6}$ for just the number of states $m_{\text{max}} \approx 200$. We note that having a finite n_{cutoff} essentially means all measurements on $H_{\text{LR-approx}}$ shall depend on an effective cutoff

length (an effective range), namely $\mathcal{L}_{\text{cutoff}}(n_{\text{cutoff}})$ (which, in principle, also depends on the system geometry and Hamiltonian control parameters), where $\mathcal{L}_{\text{cutoff}}(\infty) \to \infty$ reproduces the true thermodynamic limit. In other words, the power-law decay, appearing in Eqs. (3) and (4), would be almost exactly equivalent to the sum of exponential decays up to this $\mathcal{L}_{\text{cutoff}}$, while for longer distances (although $H_{\text{LR-approx}}$ may provide some insights on the physics of H_{LR}), the former now drops significantly faster. In fact, the cost incurred by our approximation, Eq. (4), is the introduction of a new size-dependency quantity, $\mathcal{L}_{\text{cutoff}}$ (or n_{cutoff}), where in principle one should also perform finite size scaling over $\mathcal{L}_{\text{cutoff}}$ to find the observables in the thermodynamic limit. However, our studies show that the relative changes in physical observables of our interest (other than the correlation lengths—see below) are negligible for both $H_{\text{Haldane-Shastry}}$ (on an infinite chain) and H_{LR} (on a six-leg infinite-length cylinder), when the number of kept exponentials is as large as $n_{\text{cutoff}} = 10$; this value of cutoff reproduces an effective range of *two hundreds* of lattice spacings or better, $\min[\mathcal{L}_{\text{cutoff}}] = \mathcal{O}(100)$, for both Hamiltonians.

E. Summary of our findings

We now briefly summarize our main findings. For the nearest-neighbor Hamiltonian H_{NN} of Eq. (2), on six-leg infinite-length cylinders using iDMRG with $m_{\max} = 250$, we find a phase diagram that hosts a LR-correlated three-sublattice AFM $(0.5, -0.5, 0)$-type clock order for $\Gamma \leqslant 0.75(5)$, a trivial SR-correlated x-polarized FM order for larger Γ, and a second-order phase transition separating them. The AFM ground state arises as the result of Z_2-symmetry breaking and is stabilized against the highly-degenerate classical ground state at $\Gamma = 0$ through the "order from disorder" phenomenon (induced by quantum fluctuations) as previously discussed. These results are in agreement with Refs. [46,48,50] phase diagrams.

For the LR-interacting Hamiltonian H_{LR} of Eq. (1), on six-leg infinite-length cylinders using iDMRG to optimize $H_{\text{LR-approx}}$ with $m_{\max} = 500$ and $n_{\text{cutoff}} = 10$, we find a phase diagram that exhibits three distinct ground states: (i) a LR-correlated two-sublattice Z_2-symmetry-broken AFM columnar order for low-α and low-Γ (previously unknown for the LR model), (ii) a LR-correlated three-sublattice Z_2-symmetry-broken AFM $(0.5, -0.5, 0)$-type clock order for large α and low Γ (as one should expect from the SR-correlated version of this phase on the NN model, although some features were previously unknown for the LR model), and (iii) a LR-correlated x-polarized FM order for any large Γ. Both AFM phases are expected to possess vanishing spin gaps due to the existence of robust LR correlations. The most significant difference between the detected ground states of the NN model and the LR model is that all phases of the latter exhibit LR (power-law decaying) correlations, at least for the distances comparable to their measured correlations lengths. It is important to note that due to higher computational difficulties, we do *not* provide finite size scalings with the cylinder's width for this first iDMRG study of the LR-TQIM; therefore, our provided phase diagram is only precise for the cylindrical boundary conditioned model and not essentially in the true 2D limit where width $\to \infty$. Nevertheless, our results still confirm that in ladder-type two-dimensional highly-frustrated magnets, LR quantum fluctuations always lead to LR correlations in the ground states. These results can provide directions for the future ion-trap experiments and offer some foundational understandings of the physics of LR-interacting systems. In particular, corrections to the area law of entanglement entropy are expected for such two-dimensional LR-correlated phases, as observed for their 1D counterparts.

The remainder of this paper is organized as follows. In Sec. II, we present the employed iMPS and iDMRG algorithms in further detail, covering the inclusion of LR interactions in MPOs. The structure of the triangular lattice on infinite-length cylinders and the map onto the MPS chain is explained in the same section. The calculated phase diagrams of H_{NN} and H_{LR} are displayed and extensively commented in Sec. III and Sec. IV, respectively, together with analyses of the properties of each detected ground state. In Sec. V, we conclude our findings and suggest some possible future directions.

II. METHODS

The ground state of a SR-interacting Hamiltonian on an L-site lattice with periodic boundary conditions (the translation-invariant limit will be obtained when we set $L \to \infty$) can be generally well approximated using the MPS ansatz:

$$\text{Tr} \sum_{\{s_i\}} \mathcal{A}_1^{[s_1]} \mathcal{A}_2^{[s_2]} \cdots \mathcal{A}_L^{[s_L]} |s_1\rangle \otimes |s_2\rangle \otimes \cdots \otimes |s_L\rangle, \quad (5)$$

where $\mathcal{A}_i^{[s_i]}$ is an $m \times m$ matrix that encodes all local information available to the ith state and s_i capture the local d-dimensional physical space (for example, $s_i = \{\downarrow, \uparrow\}$ and $d = 2$ for spin-1/2 particles) and m is referred to as the bond dimension of or the number of states in the MPS. The matrices $\mathcal{A}$ satisfy an orthogonality condition and can be chosen to only contain purely real values (see Refs. [27,28,30] for details). Hamiltonian operators on this L-site lattice can be analogously represented in the MPO form of

$$\sum_{\{s_i, s_i'\}} M^{s_1, s_1'} M^{s_2, s_2'} \cdots M^{s_L, s_L'} \times |s_1\rangle\langle s_1'| \otimes |s_2\rangle\langle s_2'| \otimes \cdots \otimes |s_L\rangle\langle s_L'|, \quad (6)$$

where $M_{aa'}^{ss'}$ can be thought of as a rank-4 tensor: $s, s' \in \{1, 2, \ldots, d\}$ and $a, a' \in \{1, 2, \ldots, \tilde{m}\}$, where $\tilde{m}$ is the MPO bond dimension. We note that MPOs always provide an exact representation for the physical operators (whereas MPS is only an exact representation of the state for some very special wave functions, commonly having a small finite m, or when $m \to \infty$; see Ref. [31] for examples). It is convenient to regard MPOs as $\tilde{m} \times \tilde{m}$ (super-)matrices where the elements are local operators (matrices) acting on local physical spaces. For a Hamiltonian that is a sum of finite-range interacting terms, one can write [27–29] M matrices in their Schur form (e.g., see Ref. [68]); here, we choose to present all such MPOs in their upper triangular form, since that makes it easy to read off the form of the operator from top left to bottom right. As a clarifying example, to represent the infinite sum of local operator of form $\hat{A} \otimes \hat{A} \otimes \cdots \otimes \hat{A} \otimes \hat{B} \otimes \hat{D} \otimes \hat{E} \otimes \cdots \otimes \hat{E} \otimes \hat{E}$, containing a NN two-body term, we only need a 3×3 M matrix (using transposed matrices compared with

the notation of Ref. [28]) as

$$M = \begin{pmatrix} \hat{A} & \hat{B} & \hat{0} \\ \hat{0} & \hat{0} & \hat{D} \\ \hat{0} & \hat{0} & \hat{E} \end{pmatrix}. \tag{7}$$

This can be easily extended to represent any finite-range N-body term (refer to Refs. [28,69] for more examples). In the past, such notions of MPOs have been widely used to describe finite-range interacting Hamiltonians. For example, the MPO for H_{NN} given by Eq. (2) on an arbitrary-size translation-invariant lattice corresponds to

$$M_{\text{Ising}} = \begin{pmatrix} I & S^z & \Gamma S^x \\ & 0 & S^z \\ & & I \end{pmatrix}, \tag{8}$$

where we have suppressed displaying the trivial zero elements.

Similar Schur-form MPOs can be used to represent exponentially-decaying operators in the form of the long-range stringlike terms [64]. This in turn provides one with an ansatz capable of describing power-law decaying Hamiltonians using Eq. (3). The key is in filling the additional diagonal matrix elements of a Schur-form MPO other than those identities on the edge row and column, i.e., an infinite sum of string operators in the form of $\hat{A} \otimes \hat{A} \otimes \cdots \otimes \hat{A} \otimes \hat{B} \otimes \hat{C} \otimes \cdots \otimes \hat{C} \otimes \hat{D} \otimes \hat{E} \otimes \cdots \otimes \hat{E} \otimes \hat{E}$ [here, we set no one-body field term like S^x in Eq. (8); we still assign a two-body operator set of $\hat{B}$ and $\hat{D}$, and most importantly, varying-range $\hat{C}$ operators] can be written in the MPO form of

$$M_{\text{LR}} = \begin{pmatrix} \hat{A} & \hat{B} & 0 \\ & \hat{C} & \hat{D} \\ & & \hat{E} \end{pmatrix}. \tag{9}$$

To produce the LR terms of the form in Eq. (4), but for simplicity on an infinite chain, we can set $\hat{C} = |\lambda|\hat{I}$, with $|\lambda| < 1$, $\hat{B} = \hat{S}^z$ always acting on a site numbered as $i-1$, $\hat{D} = \lambda\hat{S}^z$ always acting on a site numbered as j, and placing the identity operator elsewhere. It is straightforward to check that the resulting string operator is an infinite sum of the form $\sum_{j>i} \hat{I} \otimes \hat{I} \otimes \cdots \otimes \hat{I} \otimes \hat{S}^z_{i-1} \otimes |\lambda|^{j-i} \hat{I} \otimes \hat{I} \otimes \cdots \otimes \hat{I} \otimes \hat{S}^z_j \otimes \hat{I} \otimes \cdots \otimes \hat{I} \otimes \hat{I}$ corresponding to the Hamiltonian term of $\sum_{j>i} \lambda^{j-i} S^z_{i-1} S^z_j = \sum_{j>i} e^{\ln|\lambda|(j-i)} S^z_{i-1} S^z_j$. The extension of such LR string operators to infinite cylinders would involve summing over several chain-type terms, but otherwise is straightforward.

Let us now list the order parameters of our interest: The order parameter for a clock order can be considered as the magnitude of

$$O_{XY} = \frac{1}{N_{XY}} \left(S^z_a + e^{i\frac{4\pi}{3}} S^z_b + e^{-i\frac{4\pi}{3}} S^z_c \right), \tag{10}$$

where N_{XY} is a normalization factor, the value of which should be set according to the $S^z_{\{a,b,c\}}$ magnitudes. We note that O_{XY} is sometimes referred to as the 'XY order parameter.' We work on a translation-invariant lattice with the unit-cell size of L_u and use the following three order parameters to fully quantify the phase diagrams of both H_{NN} and H_{LR}. These order parameters are the normalized total S_x magnetization per site,

$$M^x_1 = \frac{1}{L_u} \sum_{i \in \{\text{unit-cell}\}} S^x_i \,, \tag{11}$$

suited to detect the single-sublattice FM ordering; the normalized total S_z staggered magnetizations per site,

$$M^z_2 = \frac{1}{L_u} \sum_{i \in \{\text{unit-cell}\}} (-1)^i S^z_i \,, \tag{12}$$

suited to detect the two-sublattice AFM columnar ordering, and XY order parameter per site,

$$M^z_3 = \frac{1}{L_u \times N_{XY}} \sum_{a,b,c \in \{\text{unit-cell}\}} S^z_a + e^{i\frac{4\pi}{3}} S^z_b + e^{-i\frac{4\pi}{3}} S^z_c \,, \tag{13}$$

suited to detect the three-sublattice AFM clock ordering.

Returning to the iMPS construction of the model, after building M_{LR}-type MPOs for Eq. (1) and finite-range ones for Eq. (2), we then optimize the corresponding MPS using the iDMRG algorithm, such that the reduced density matrices will then satisfy fixed-point equations. We then use the method of the *transfer operator*, $\mathcal{T}_I$, as explained in Refs. [28,29,70] (we note that the original 'transfer matrix' scheme was introduced for MPS in Refs. [71,72]), to find the energies per site as well as the expectation values of magnetizations per site, M^x_1, M^z_2, and M^z_3. We note that on an infinite lattice the elements of M matrices would diverge, however, the expectation values per site are well defined, and the principal correlation length, $\xi(m)$, can be measured from the spectrum of $\mathcal{T}_I$ (ξ is always measured per Hamiltonian unit-cell size, but due to the cylindrical form of the lattice can be thought to represent the typical long-direction size 'per lattice spacing'). Moreover, to avoid the requirement of the extra normalization [73] needed for some α values (when considering the thermodynamic limit or studying the scaling behavior of finite-size observables), we confine ourselves to $\alpha > 1$, where the thermodynamic limit is well defined without additional normalization. Finally, we note that due to the current limitations of the iDMRG algorithm, we were unable to directly calculate the bulk spin gap for any of the presented ground states in this paper.

As is clear from Eq. (5), MPS is inherently a 1D ansatz. Therefore, DMRG simulations in 2D require a mapping between the MPS chain and the physical lattice. Unavoidably, this means that interactions in the 2D lattice map to couplings that are at least as long range, but often longer range, on the 1D MPS chain. We use an 'efficient' mapping for the MPS onto an infinite-length 2D lattice [i.e., $L_x \to \infty$ and L_y is finite, where $L_x(L_y)$ always denotes long-(short-)direction size], as demonstrated in Fig. 5.2(a) of Ref. [69] and detailed in its corresponding section (see also below). This particular mapping minimizes the range of finite-range couplings in the resulting 1D Hamiltonian. Furthermore, there exists an infinite number of ways to wrap a 2D lattice to create a generic periodic boundary condition in the Y direction. The wrapping creates an infinite-length cylinder, one which is generally twisted. The use and classification of such cylindrical boundary conditions are common practice in the study of single-wall carbon nanotubes (e.g., see Ref. [74]). To identify the wrappings of the triangular lattice on an infinite cylinder, we use this standard but versatile

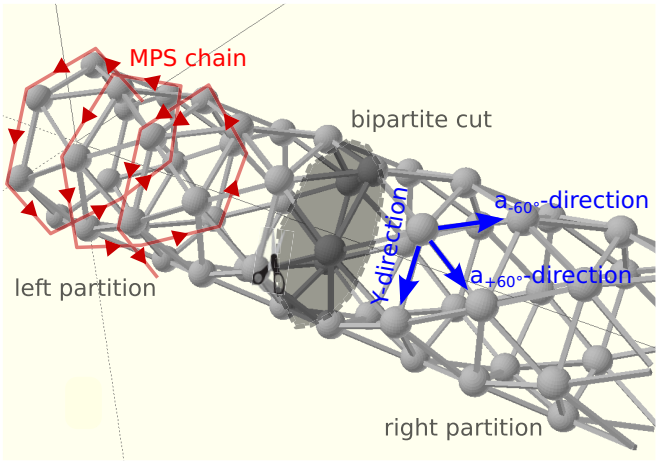

FIG. 1. Cartoon visualization of a triangular lattice on a YC6 cylinder. Spins sit on spheres. An 'efficient' mapping of the MPS chain is shown using the red spiral. The green arrows represent the unit vectors on three principal lattice directions. The transparent gray plane corresponds to the bipartite cut that creates a left and right partition, without crossing any Y-direction bond, and is used to calculate bipartite iDMRG quantities.

classification, where the corresponding notations are detailed in Chap. 2 of Ref. [69]. The majority of our calculations are performed on the highly convenient and computationally beneficial infinite-length YC6 structures with the shortest possible wrapping vector as $\mathbf{C}_0[\text{YC6}]=(6,-6)$ in the unit of $(\mathbf{a}_{+60^\circ},\mathbf{a}_{-60^\circ})$ [see Fig. 1—in this paper, we represent the unit vectors of inverse lattices, $(\mathbf{K}_x,\mathbf{K}_y)$, in correspondence to the $(\mathbf{a}_{+60^\circ},\mathbf{a}_{-60^\circ})$ notation]. Some benefits of the YC structure include having the same circumferences as the short-direction size of L_y, iDMRG Hamiltonian unit-cell aligning in the $\mathbf{C}_0$ direction, and providing high-resolving power for the spectrum of reduced density matrix while respecting the bipartite and tripartite lattice symmetries with some nonexcessive wave function unit-cell sizes. A generic YC6 structure is demonstrated in Fig. 1, where we also display the MPS efficient mapping method. We reiterate that, on the cylinder, such mapping provides the shortest one-dimensional SR coupling ranges over the periodic boundary condition connections. To study the effect of the lattice geometry on detected phases, we perform few additional iDMRG calculations on distinctly wrapped systems, namely XC6 structures with $\mathbf{C}_0[\text{XC6}]=(6,6)$ and six-leg three-site unit-cell structures with $\mathbf{C}_0[\text{three-site}]=(6,-2)$, for some control parameters of interest (see below for details).

In practice, we find the phase diagram of the Hamiltonian H_{LR} of Eq. (1) mainly by performing an extensive series of ground state iDMRG simulations on YC6 structures for $\alpha=[1.1,4.0]$ and $\Gamma=[0.1,1.5]$, having a resolving power as small as $\Delta\alpha,\Delta\Gamma=0.05$ and maximum MPS bond dimension of $m_{\text{max}}=500$. We used a 10-term expansion ($n_{\text{cutoff}}=10$) of the form Eq. (3) to translate exponential decays, produced by the MPO of Eq. (9), into LR interactions. We reiterate that our Hamiltonian reconstruction and validation tests proved that a 10-term expanded $H_{\text{LR-approx}}$ of the form Eq. (4) can faithfully describe (before terms start to fall exponentially rapidly) the original Hamiltonian, H_{LR}, on the YC6 structure, typically, up to *few hundreds* of lattice spacings (the exact value of $\mathcal{L}_{\text{cutoff}}$ depends on the assigned Hamiltonian control parameters). The selection of $L_y=6$ is mainly due to the simplicity as this is the smallest width for which the YC structure can be set to respect the Y-axis bipartite and the tripartite symmetries. However, we note that $L_y=6$ is large enough to produce a phase diagram exhibiting exclusively two-dimensional phase phenomena, some of which are distinct from the phase properties observed in the 1D long-range quantum Ising model [45]. Additionally, we remind that our width-6 results are a first attempt to create an iMPS/iDMRG phase diagram for this model (or any two-dimensional LR-interacting spin system). As mentioned, we also study the LR-TQIM on XC6 and $\mathbf{C}_0[\text{three-site}]=(-3,3)$ systems for $(\alpha,\Gamma,m_{\text{max}})=(1.5,0.2,100)$ (predicted to lie deep inside the LR columnar phase region—see below) and a series of very large α and small Γ values with $m_{\text{max}}=250$ [predicted to lie deep inside $(0.5,-0.5,0)$ clock phase region—see below]. Our results show that the energy per site and real-space correlation patterns are the same in comparison to the equivalent points on YC6 systems up to the machine precision. These results confirm that the stabilization of multipartite ground states of LR-TQIM is independent of the geometry, i.e., the choice of the wrapping structure hosting the triangular lattice. For obtaining the phase diagram of H_{NN}, we perform conventional finite-range iDMRG calculations associated with the MPO Eq. (8) for 11 chosen points distributed unevenly in $\Gamma=(0,2.0)$, while keeping up to $m_{\text{max}}=250$ number of states.

III. PHASE DIAGRAM OF THE NN MODEL

Is this section, we present the iDMRG phase diagram of the NN-TQIM, with Hamiltonian given by Eq. (2), on six-leg cylinders in Fig. 2, where the S^x magnetization (M_1^x), staggered S^z magnetization (M_2^z), and XY magnetization (M_3^z) per site are plotted. For the majority of Γ points, the extrapolations toward the thermodynamic limit of $m\to\infty$ are performed linearly with $\sqrt{\varepsilon_m}$, where ε_m is the average truncation error of iDMRG for a fixed-m sweep, as it was suggested by White and Chernyshev [75] for observables other than the energy (recall that $m\to\infty$ corresponds to $\varepsilon\to 0$ limit). However, since the scaling behaviors of observables vary unpredictably in the vicinity of a critical point or deep inside a phase region that is paramagnetic with respect to the target order parameter, it was not possible to perform such extrapolations everywhere. For these points, we observed that the decay of the order parameters are too rapid and/or the individual values are too small (in order of the machine epsilon). We replace $M^{\{(x),z\}}_{\{(1),2,3\}}(m\to\infty)$ with $M^{\{x,z\}}_{\{(1),2,3\}}(m_{\text{max}})$, virtually implying zero uncertainty for these points. Four examples of individual magnetization values are presented in Fig. 3, where two subfigures correspond to large individual values of magnetizations, deep inside matching phase regions where a linear fit versus $\sqrt{\varepsilon_m}$ works well, while other subfigures correspond to Γ close to a predicted critical point and/or where magnetizations are decaying too fast, and so no analytical fit is applicable. Using this approach, we estimate that the critical point of the NN model lies on $\Gamma_c=0.75(5)$, i.e., the first point that M_3^z touches the zero axis. This corresponds to a second-order quantum phase transition, due to observed

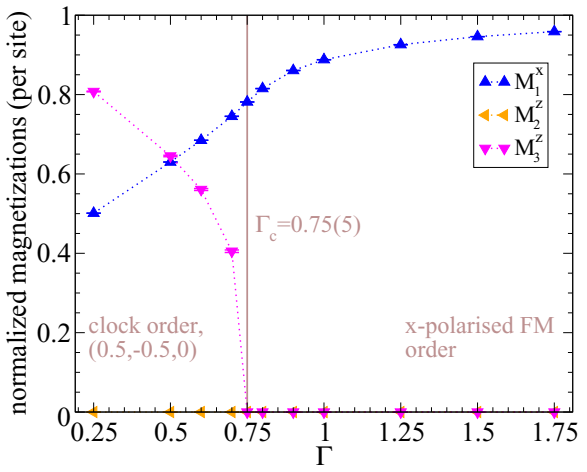

FIG. 2. iDMRG phase diagram of NN-TQIM, Eq. (2), on a YC6 structure. Filled triangular symbols with error bars show the thermodynamic-limit magnetizations per site, $M_1^x(m\to\infty)$, $M_2^z(m\to\infty)$, and $M_3^z(m\to\infty)$ (cf. Eqs. (11), (12), and (13), respectively), extrapolated using a linear fit versus $\sqrt{\varepsilon_m}$ (see below for some examples on individual fits). We set $N_{xy}=\frac{1}{\sqrt{12}}$ for M_3^z [as appeared in Eq. (10)], which is the maximum value achievable for an ideal $(0.5,-0.5,0)$ ordering. The symbols with no error bars stand for $M_2^z(m_{\max})$ and $M_3^z(m_{\max})$, where no analytical fit was possible toward the thermodynamic limit of $m\to\infty$ (due to extreme decay and/or smallness of observables). Pointed lines only connect symbols as guides for the eyes.

continuous changes in the values of magnetizations which are caused by the quantum fluctuations. The critical point of the model on YC6 triangular-lattice structures is relatively

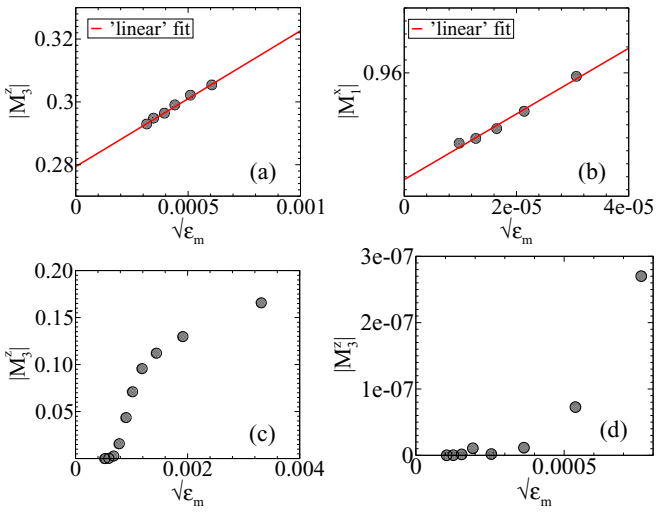

FIG. 3. Examples for the individual order parameter values of the ground states of NN-TQIM, Eq. (2), on YC6 structures: (a) M_3^z at $\Gamma=0.5$ [deep inside $(0.5,-0.5,0)$-ordered clock phase region], (b) M_1^x at $\Gamma=1.75$ (deep inside x-polarized FM region), (c) M_3^z at $\Gamma=0.75$ (close to the critical point), and (d) M_2^z at $\Gamma=1.00$ (deep inside x-polarized FM region). Evidently, for (a) and (b), rigorous linear extrapolations versus $\sqrt{\varepsilon_m}$ are possible, while not for others due to extreme decay of individual magnetizations and their convergence toward small values of order of the machine epsilon.

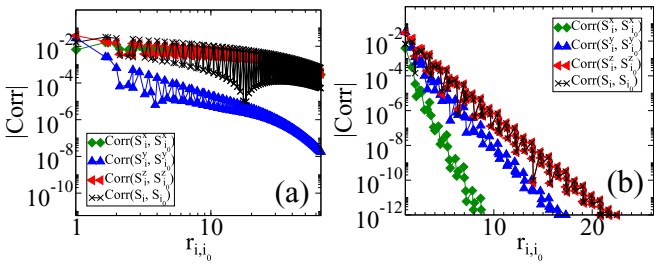

FIG. 4. The scaling of the connected correlation functions, $\mathrm{Corr}(S_i^{\{x,y,z\}},S_{i_0}^{\{x,y,z\}})$, versus real-space chord distance, r_{i,i_0}, for the iDMRG ground states of NN-TQIM, Eq. (2), on YC6 structures at (a) $\Gamma=0.25$ [deep inside "order from disorder"-induced $(0.5,-0.5,0)$ clock phase region] in *linear-log* scale and (b) $\Gamma=1.5$ [deep inside SR-correlated x-polarized FM phase region] in *full-logarithmic* scale.

close to $\Gamma_c\approx 0.705$ [in our Hamiltonian notation of Eq. (2)] predicted by Penson *et al.* [50] and $\Gamma_c\approx 0.825$ by Isakov and Moessner [48] (see also Sec. I). For $\Gamma<0.75(5)$, $M_3^z(m\to\infty)$ values are finite and large, while $M_1^x(m\to\infty)[M_2^z(m\to\infty)]$ values are relatively (very) small, which suggests the phase is a three-sublattice AFM clock $(0.5,-0.5,0)$ order (see below for detailed properties). The convergence of iDMRG ground states to such a $(0.5,-0.5,0)$ order is consistent with the proposed ground state from Refs. [46,48]. For $\Gamma\geqslant 0.75(5)$, $M_2^z(m_{\max})$ and $M_3^z(m_{\max})$ are vanishing while $M_1^x(m\to\infty)$ values are finite and large (but not equal to unity). This behavior suggests the phase is a partially x-polarized FM order, or a paramagnet considering the z polarizations, as one expects.

We scrutinize the properties of detected ground states of H_{NN} by considering some more iDMRG observables in the following list:

(1) $0<\Gamma\leqslant 0.75(5)$, the "order from disorder"-induced clock $(0.5,-0.5,0)$ order: The ground state is a Z_2-symmetry-broken three-sublattice order and exhibits an AFM arrangement of spins in a triangular plaquette according to $(0.5,-0.5,0)$, or $(\uparrow,\downarrow,\rightarrow)$, which has a zero net magnetization. The existence of this long-range spin ordering is evident from finite and large $M_3^z(m\to\infty)$ values that appeared in Fig. 2; in addition, we verified the $(0.5,-0.5,0)$ structure by studying the real-space visualization of correlation functions (not presented here). In Sec. I C, we have learned that the classical ground state ($\Gamma=0$) is a macroscopically-degenerate LR-correlated disordered phase, where quantum-to-classical mapping implies that the finite-temperature states choose a LR-correlated three-sublattice order induced by classical version of "order from disorder" phenomenon. We argue that the ground state of NN-TQIM for $0<\Gamma\leqslant 0.75(5)$ is the quantum analog of this finite-temperature phase, where one needs to replace the temperature with Γ ("order from disorder" is now induced by quantum fluctuations) consistent with Refs. [46,48,50]. Our results confirm that the clock order is LR correlated as observed from the *almost* algebraic decays of two-point *connected* correlation functions, $\mathrm{Corr}(S_i^{\mathfrak{a}},S_{i_0}^{\mathfrak{a}})=\langle S_i^{\mathfrak{a}}S_{i_0}^{\mathfrak{a}}\rangle-\langle S_i^{\mathfrak{a}}\rangle\langle S_{i_0}^{\mathfrak{a}}\rangle$, $\mathfrak{a}\in\{x,y,z\}$ [and defining $\mathrm{Corr}(\mathbf{S}_i,\mathbf{S}_{i_0})=\mathrm{Corr}(S_i^x,S_{i_0}^x)+\mathrm{Corr}(S_i^y,S_{i_0}^y)+\mathrm{Corr}(S_i^z,S_{i_0}^z)$], shown in Fig. 4(a) for $\Gamma=0.25$. Note that in the figure, which belongs to a $m=250$ wave function, it may appear that for long distances the correlators start to drop exponentially fast; however, we suggest this is a

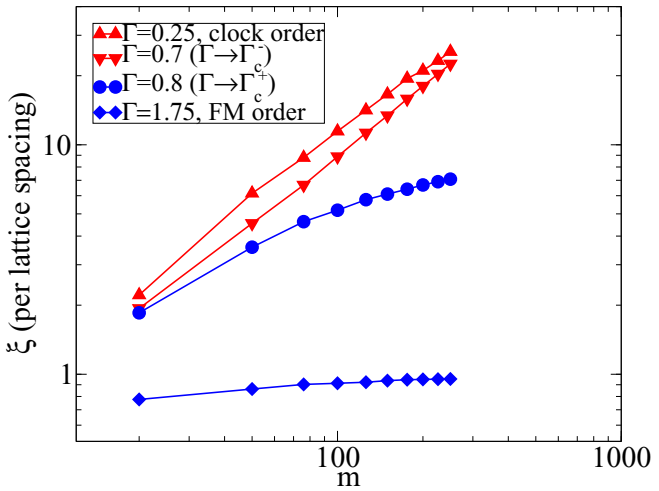

FIG. 5. iDMRG correlation lengths for the ground states of NN-TQIM, Eq. (2), on YC6 structures for a selection of Γ points.

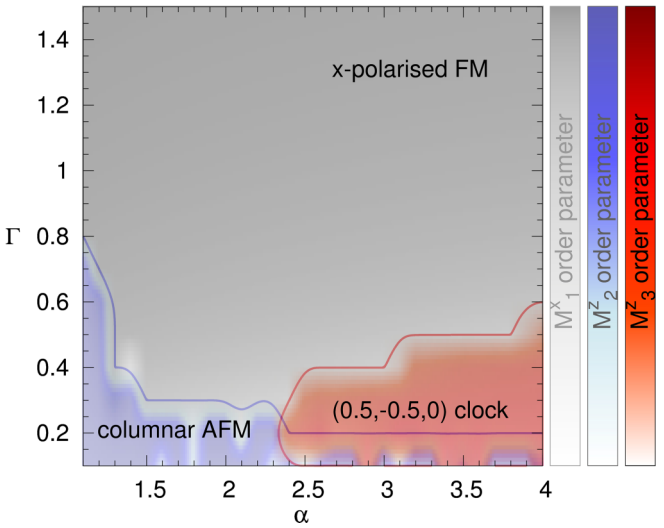

FIG. 6. iDMRG phase diagram of LR-TQIM, Eq. (1), on a YC6 structure. This shows the combined color map of measured magnetizations per site, namely M_1^x, M_2^z, and M_3^z [cf. Eqs. (11), (12), and (13), respectively—we set $N_{xy} = \frac{1}{\sqrt{12}}$ for M_3^z as appeared in Eq. (10)]. The color intensity of all palettes vary in the range of [0,1], as expected for normalized order parameters. The thick blue (red) line is the zero-value (while taking into account the maximal uncertainty in measurements of the magnetizations) contour line specifying the phase boundary between the LR-correlated columnar order [clock $(0.5, -0.5, 0)$ order] and other ground states. Here, for the majority of (α,Γ) points, we insert the thermodynamic-limit magnetizations, $M_1^x(m \to \infty)$, $M_2^z(m \to \infty)$, and $M_3^z(m \to \infty)$, which are extrapolated using a linear fit versus $\sqrt{\varepsilon_m}$ (see below for some examples on individual fits). However, where no analytical fit is possible (due to extreme decay and/or smallness of observables), we instead insert $M_1^x(m_{\max})$, $M_2^z(m_{\max})$, and $M_3^z(m_{\max})$ as needed.

finite-m effect and for $m \to \infty$, there should exist a perfect power-law decay. When we decreased the number of states, the exponential-drop tail did appear and always at shorter distances. Moreover, a power-law growth of correlation lengths versus m is observed for this order as shown in Fig. 5 for $\Gamma = 0.25$. Although this ground state resembles 1D critical phases by possessing an algebraic increase of the correlation lengths up to $\xi(m_{\max}) \sim O(10)$ per Hamiltonian unit-cell size, we predict its stabilization here is an inherently 2D phenomenon.

(2) $\Gamma \geqslant 0.75(5)$, the SR-correlated x-polarized FM order: The observed ground state exhibit partially polarized spins that are ferromagnetically aligning in spin's x direction while possessing vanishing magnetization (i.e., exhibiting paramagnetism) in other directions. We verified the FM structure by observing finite and large values of $M_1^x(m \to \infty)$ (nonzero net magnetization) and vanishing values of $M_2^z(m_{\max})$ and $M_3^z(m_{\max})$ as shown in Fig. 2. This was also supported through visualizations of real-space correlation functions (not presented here). The FM order is SR correlated due to exponentially-decaying connected correlators, as shown in Fig. 4(b) for $\Gamma = 1.5$, and therefore gapped and SR entangled due to small and saturating correlation lengths (when plotting versus m), as shown in Fig. 5 for, e.g., $\Gamma = 1.75$.

IV. PHASE DIAGRAM OF THE LR MODEL

The fully-quantitative iDMRG phase diagram of LR-TQIM, with Hamiltonian given by Eq. (1), is presented in Fig. 6. This figure displays the three normalized order parameters of interest, i.e., M_1^x, M_2^z, and M_3^z [cf. Eqs. (11), (12), and (13), respectively], corresponding to the stabilization of three observed ground states: LR-correlated x-polarized FM, LR-correlated columnar AFM, and LR-correlated clock $(0.5, -0.5, 0)$ order, respectively.

Analogous to the NN phase diagram shown in Fig. 2, for the majority of control parameters in Fig. 6 it was possible to perform the linear extrapolation of the magnetizations versus $\sqrt{\varepsilon_m}$ toward the thermodynamic limit of $m \to \infty$; however, as before, typically close to critical lines or deep inside a paramagnetic phase (with respect to the targeted order parameter), there exist some points where no analytical fit is possible due to extreme decays of order parameters and/or exhibiting magnitudes as small as the machine epsilon. In such cases, we replace $M^{\{(x),z\}}_{\{(1),2,3\}}(m \to \infty)$ with $M^{\{(x),z\}}_{\{(1),2,3\}}(m_{\max})$ implying strictly zero uncertainties. For some examples, Fig. 7 illustrates four plots of individual magnetizations with some different scaling behaviors.

In the phase diagram, Fig. 6, the two contour lines provide our estimations for the phase boundaries. All are predicted to be second order phase transitions. Briefly, strong x-polarized FM order exists for large Γ regardless of the values of α, columnar order exists for small α and Γ, and $(0.5, -0.5, 0)$-type clock order exists for large α and small Γ. In addition, the coexistence of a weak columnar and a weak $(0.5, -0.5, 0)$ order observed for $\alpha \geqslant 2.40(5)$ and $\Gamma \leqslant 0.20(5)$.

The recent mean-field/QMC study [62] of the model similarly found a three-region semiquantitative phase diagram having phase transition lines relatively close to our predictions. We note two points of distinction in our conclusions. First, Humeniuk [62] does not discuss the nature of the ground state for small α and Γ (it is labeled in Ref. [62] as a 'classical phase'). Second, for large α and small Γ, they find a different type of clock phase, specifically, the $(0.5, -0.25, -0.25)$ ordering (the so-called 120°-ordered arrangement on a

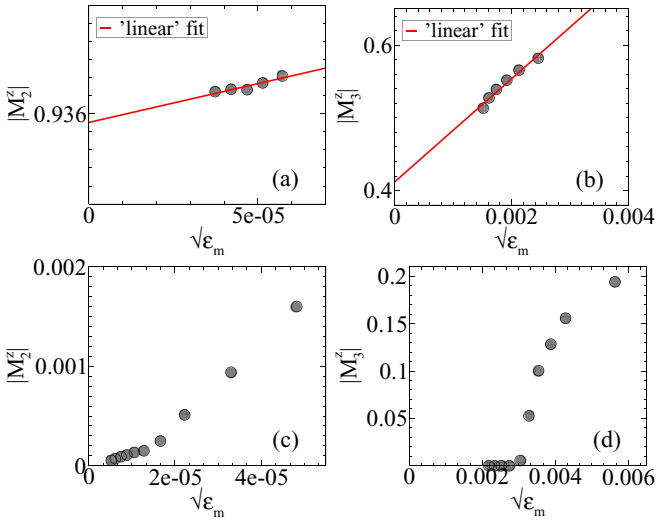

FIG. 7. Examples for the individual order parameter values for the ground states of LR-TQIM, Eq. (1), on YC6 structures: (a) M_2^z at $(\alpha,\Gamma) = (1.6,0.2)$ (deep inside columnar AFM phase region), (b) M_3^z at at $(\alpha,\Gamma) = (2.6,0.3)$ [deep inside $(0.5, -0.5,0)$ clock phase region], (c) M_2^z at $(\alpha,\Gamma) = (1.5,0.3)$ (close to a critical point), and (d) M_3^z at $(\alpha,\Gamma) = (2.2,0.3)$ (close to a critical point). Evidently, for (a) and (b), rigorous linear extrapolations versus $\sqrt{\varepsilon_m}$ are possible, while not for others due to extreme decay of individual magnetizations and their convergence toward small values of order of the machine epsilon.

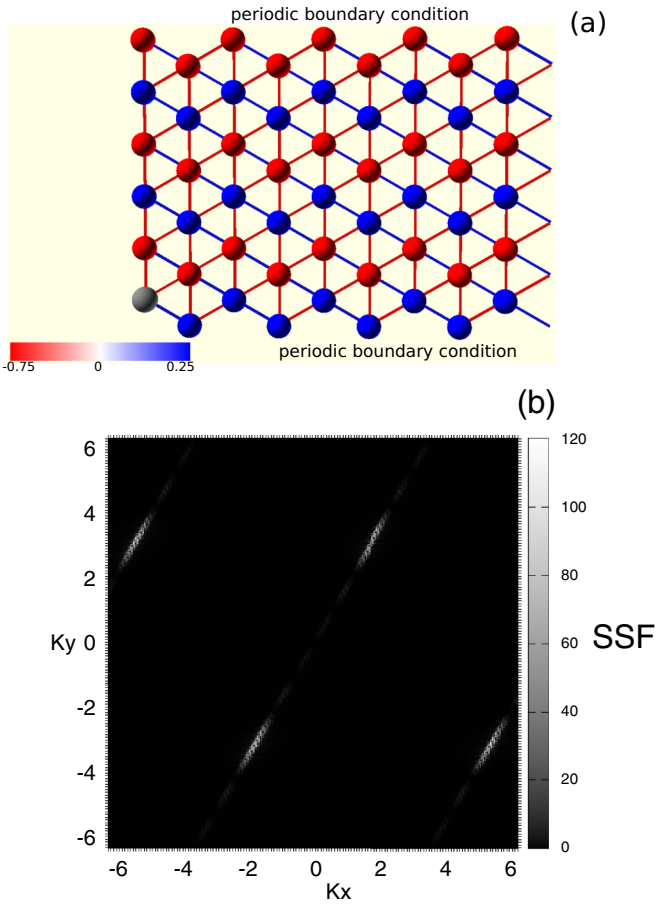

FIG. 8. Lattice visualizations for the iDMRG ground state of the LR-TQIM, Eq. (1), on an YC6 structure at $(\alpha,\Gamma) = (1.2,0.3)$ (LR-correlated columnar order). (a) S^z-S^z correlation functions for up to nine legs of the infinite cylinder. The size and the color of the spheres indicate the (long-range) spin-spin correlations in respect to the principal (gray) site, and the thickness and the color of the bonds indicate the strength of the NN correlations. (b) SSF, where we present the Bragg-type peaks within the first and second Brillouin zones of the inverse lattice.

triangular plaquette), in contrast to our results. Importantly, the stabilization of the clock $(0.5, -0.5,0)$ order on the NN model is confirmed by Sec. III and Ref. [46] results for small Γ; the LR model *must* reproduce the H_{NN} ground state for $\alpha \to \infty$. Moreover, for large α and vanishing Γ, although we already know that in the thermodynamic limit there exists a macroscopically-degenerate finite-entropy classical ground state and any *finite* Γ would allow quantum fluctuations to choose a distinct phase [as for $(0.5, -0.5,0)$ order of H_{NN} or large-α order of $H_{\rm LR}$] through "order from disorder" (cf. Sec. I). But, on the restricted geometry of the YC structure, it appears the classical ground states are distinct: Employing full diagonalization calculations for classical $H_{\rm LR}$ $(\Gamma = 0)$ on small $L_x = 3,4$-length YC6 systems, for all α, we detect a product-state columnar order as the lowest energy state. We scrutinize the properties of detected ground states of $H_{\rm LR}$ by considering some more iDMRG observables in the following subsections.

A. The LR-correlated columnar AFM ordered phase

We now investigate the properties of the LR-correlated columnar AFM order, which is the 'blue' region in Fig. 6. The ground state is a two-sublattice Z_2-symmetry-broken AFM columnar (or stripe) order. The phase is columnar in the sense that there exist FM columns (or stripes) spiraling the cylinder in the long direction. The columnar order is twofold degenerate (e.g., see Ref. [70]) on large-width YC-structured triangular lattices as the FM stripes can be aligned either in $\mathbf{a}_{+60^\circ}$ or $\mathbf{a}_{-60^\circ}$ directions (see Fig. 1—we note that one can always set the iDMRG unit-cell size such that the state converges to the arrangement that has $\mathbf{a}_{+60^\circ}$-aligned FM stripes). It is noteworthy that columnar order is, in principle, threefold degenerate in the true 2D limit [76], as the FM stripes can also align in the lattice Y direction; however, on YC structures with a large enough width, such iDMRG ground states possess higher energies per site compared to the two other alignments. We verified the columnar-ordered nature of spins for this region by observing the large finite values of $M_2^z(m \to \infty)$ [vanishing values of $M_1^x(m_{\rm max})$ and $M_3^z(m_{\rm max})$], (cf. Fig. 6) and the real-space visualization (projected into a plane) of calculated S^z-S^z correlation functions, as pictured in Fig. 8(a) for $(\alpha,\Gamma) = (1.2,0.3)$. Furthermore, in Fig. 8(b), we verify the sublattice structure of the columnar order at $(\alpha,\Gamma) = (1.2,0.3)$ by calculating the static spin structure factor (static SSF) of S^z-S^z correlations, $\mathrm{SSF}(\mathbf{k}, N_{\rm cutoff}^{\rm SSF}) = \frac{1}{N_{\rm cutoff}^{\rm SSF}} \sum_{i,i'}^{N_{\rm cutoff}^{\rm SSF}} \langle S_i^z S_{i'}^z \rangle e^{i\mathbf{k}\cdot(\mathbf{r}_i - \mathbf{r}_{i'})}$, for large cutoff, $N_{\rm cutoff}^{\rm SSF} \gg 1$, set as the upper limit for site numbers (see [70] for the details of our approach to measure the SSF for iDMRG wave functions; in particular, here $\mathbf{r}_i$ denotes the position vector of a spin S_i^z in the *planar* map of the periodic lattice). In Fig. 8(b),

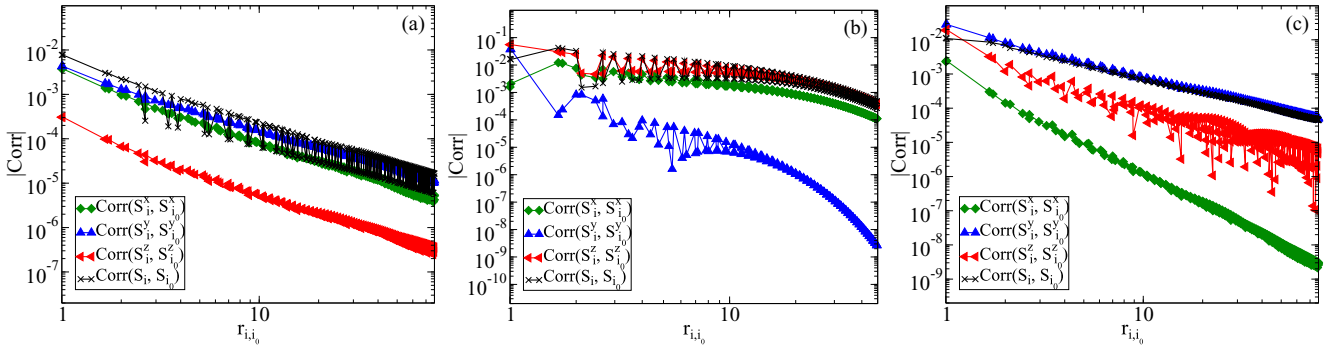

FIG. 9. The scaling of the connected correlation functions, $\mathrm{Corr}(S_i^{\{x,y,z\}}, S_{i_0}^{\{x,y,z\}})$, versus real-space chord distance, r_{i,i_0}, for the iDMRG ground states of LR-TQIM, Eq. (1), on infinite YC6 structures at (a) $(\alpha,\Gamma) = (1.2,0.3)$ [deep inside LR-correlated columnar phase region], (b) $(\alpha,\Gamma) = (4.0,0.3)$ [deep inside LR-correlated $(0.5, -0.5, 0)$ clock phase region], and (c)$(\alpha,\Gamma) = (1.2,1.5)$ [deep inside LR-correlated x-polarized FM phase region]. Plots are in *full-logarithmic* scales.

the existence of an equilateral parallelogram-shaped inverse lattice that surrounds the first Brillouin zone and exhibits four strong Bragg-type peaks, is definitive evidence for the columnar arrangement of spins. Figure 8(b) predicts the wave vector of $\mathbf{Q} = (\pm 1.86(6), 3.12(4))$ for this phase, which is quite close to the expected vector of $\mathbf{Q}^{\mathrm{theory}}_{\mathrm{columnar}} = (\pm\pi/\sqrt{3}, \pi) \approx (\pm 1.81, 3.14)$.

The SR-correlated version of the columnar order was previously observed as the ground state of the J_1-J_2 triangular Heisenberg model on the YC structures [70,77–79], which emerges from continuous symmetry breaking for large positive J_2/J_1 (considering antiferromagnetic J_1). The properties of the columnar order of H_{LR} are virtually the same as this SR-correlated columnar phase, except, importantly, we discovered that for the former, the LR quantum fluctuations in the Hamiltonian leads to *LR correlations*. This is evident from the power-law decay of connected correlation functions as shown in Fig. 9(a) for $(\alpha,\Gamma) = (1.2,0.3)$. In addition, the columnar order is LR entangled due to possessing large correlation lengths as shown in Fig. 10 for $(\alpha,\Gamma) = (1.2,0.3)$. We note that the saturation of correlation lengths (versus m) for considered

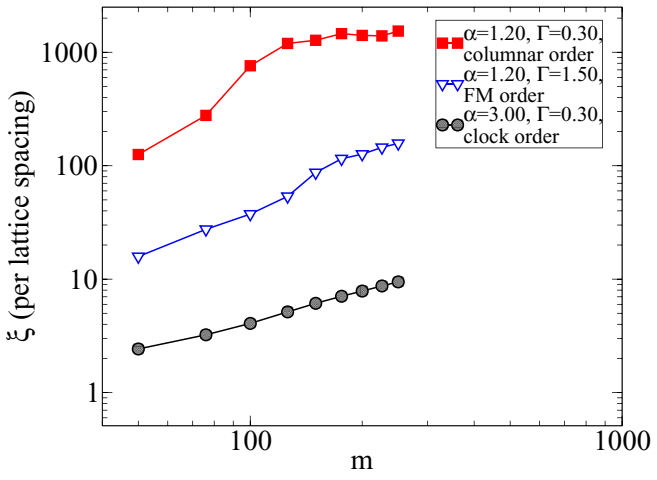

FIG. 10. iDMRG correlation lengths for the ground states of LR-TQIM, Eq. (1), on infinite YC6 structures for a selection of (α,Γ) points.

control parameters are only due to the existence of a finite n_{cutoff} in our LR to exponential-decaying couplings approximation, Eq. (3), and does not convey any physical meaning. This would be eventually true for any correlation length curves of types plotted in Fig. 10, in case one continues to find ξ values for larger-m ground states. Nevertheless, although we have not measured the spin gap directly, the columnar phase has coexistence of magnetic ordering and power-law correlations due to the LR interactions, and hence we expect that the spectrum is gapless.

B. The LR-correlated clock $(0.5, -0.5, 0)$-ordered phase

We now turn to the LR-correlated clock $(0.5, -0.5, 0)$ order, shown as the 'red' region of Fig. 6. The ground state is a three-sublattice Z_2-symmetry-broken clock order arranged antiferromagnetically on a triangular plaquette according to $(0.5, -0.5, 0)$, which exhibits LR correlations and LR entanglement. The sublattice properties of the $(0.5, -0.5, 0)$ order of H_{LR} are *exactly* the same as the LR-correlated clock order of the NN model, Sec. III, except that the LR correlations are now predicted to be (at least partly) induced by LR interactions in H_{LR}. We verified the sublattice structure of the LR-correlated clock order using the measurement of large finite values of $M_3^z(m \to \infty)$ [vanishing values of $M_1^x(m_{\max})$ and $M_2^z(m_{\max})$]—see Fig. 6. We performed visualizations of real-space correlations, as shown in Fig. 11(a) for $(\alpha,\Gamma) = (3.0,0.3)$, and calculating the SSF, as shown in Fig. 11(b), at the same point. In Fig. 11(b), the existence of a hexagonal-shaped inverse lattice that surrounds the first Brillouin zone and exhibits six strong Bragg-type peaks shows that there is a three-sublattice arrangement of the spins. Figure 11(b) predicts the wave vector of $\mathbf{Q} \approx (\pm 3.61(5), \pm 2.06(6))$ for this phase, which is quite close to the expected vector of $\mathbf{Q}^{\mathrm{theory}}_{\mathrm{clock}} = (\pm 2\pi/\sqrt{3}, \pm 2\pi/3) \approx (\pm 3.63, \pm 2.09)$. Furthermore, we verified the LR-correlated nature of the phase by observing power-law decay of connected correlators (at least for short distances) as demonstrated for $(\alpha,\Gamma,m) = (4.0,0.3)$ in Fig. 9(b). As in Fig. 4(a) for the NN model, in Fig. 9(b) (which belongs to a $m = 250$ wave function), it seems that the correlator tails drop exponentially fast; we again argue that this is a finite-m phenomenon and for $m \to \infty$, one would recover an ideal algebraic decay (when we decreased the number of

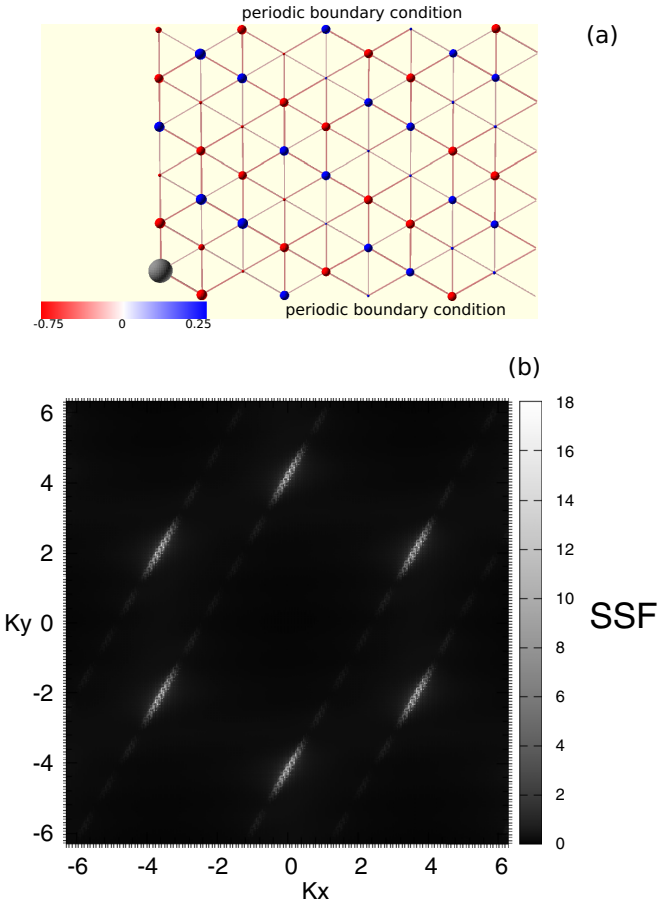

FIG. 11. Lattice visualizations for the iDMRG ground state of the LR-TQIM, Eq. (1), on an YC6 structure at $(\alpha,\Gamma) = (3.0,0.3)$ [LR-correlated clock $(0.5, -0.5,0)$ order]. (a) S^z-S^z correlation functions for up to nine legs of the infinite cylinder. The size and the color of the spheres indicate the (long-range) spin-spin correlations in respect to the principal (gray) site, and the thickness and the color of the bonds indicate the strength of the NN correlations. (b) SSF, where we present the Bragg-type peaks within the second Brillouin zone of the inverse lattice.

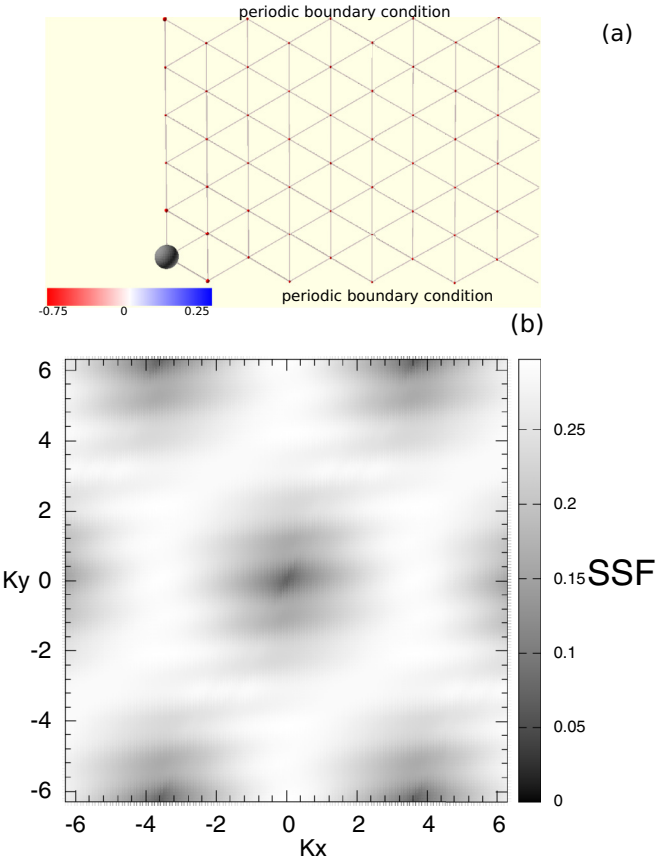

FIG. 12. Lattice visualizations for the iDMRG ground state of the LR-TQIM, Eq. (1), on an YC6 structure at $(\alpha,\Gamma) = (1.2,1.5)$ (LR-correlated FM order). (a) S^z-S^z correlation functions for up to nine legs of the infinite cylinder. The size and the color of the spheres indicate the (long-range) spin-spin correlations in respect to the principal (gray) site, and the thickness and the color of the bonds indicate the strength of the NN correlations. (b) SSF, where there are no Bragg-type peaks present within the first and second Brillouin zones of the inverse lattice.

states, the exponential-drop tail started to appear, always, at shorter distances). Moreover, the ground state is LR entangled due to exhibiting a power-law increase of correlation lengths, as shown in Fig. 10 for $(\alpha,\Gamma) = (3.0,0.3)$, which goes up to $\xi(m_{\max}) = O(10)$ per Hamiltonian unit-cell size (however, we reiterate that the correlation lengths can still start to saturate for larger m). At last, we expect the LR-correlated clock $(0.5, -0.5,0)$ order to be gapless due to the same reasoning provided for the gap nature of the LR-correlated columnar ground states.

C. The LR-correlated x-polarized FM ordered phase

Finally, we analyze the LR-correlated x-polarized FM order, shown as the 'gray' region of Fig. 6. The ground state is a ferromagnet with spins exhibiting partial polarizations in spin's x direction and paramagnetic in other directions, while possessing LR correlations and LR entanglement. The spin alignment properties of the FM order of $H_{\rm LR}$ are virtually the same as the FM order of the NN model, Sec. III, except, importantly, the former is LR correlated. We verified the FM arrangement of the spins in the ground state by measuring large finite values of $M_1^x(m \to \infty)$ [i.e., nonzero net magnetization; also, $M_2^z(m_{\max})$ and $M_3^z(m_{\max})$ are vanishing in this region], cf. Fig. 6, visualization of real-space correlations, as shown in Fig. 12(a) for $(\alpha,\Gamma) = (1.2,1.5)$, and calculating the SSF, as shown in Fig. 12(b) for the same point. In Fig. 12(b), there are no significant Bragg-type peaks within the first and second Brillouin zones (the SSF is featureless in this sense) that verifies the paramagnetic nature of the FM order considering S^z-S^z correlations. Furthermore, we verified the LR-correlated nature of the phase by observing power-law decay of connected correlators as demonstrated for $(\alpha,\Gamma) = (1.2,1.5)$ in Fig. 9(c). Moreover, the LR-entangled nature of the ground state is clear from the power-law increase of correlation lengths, as shown in Fig. 10 for $(\alpha,\Gamma) = (1.2,1.5)$ [the correlation lengths are increasing to values as large as $\xi(m_{\max}) = O(1000)$ per Hamiltonian unit-cell size, and then, saturate due to the existence of a finite $\mathcal{L}_{\rm cutoff}$].

V. CONCLUSION AND OUTLOOK

We have exploited the latest developments in iMPS and iDMRG algorithms [28,29,64] to calculate fully-quantitative phase diagrams of NN- and LR-interacting triangular Ising models in a transverse field on six-leg infinite-length cylinders. The phase diagram of the NN model contains a LR-correlated clock $(0.5, -0.5, 0)$ order, a partially-polarized SR-correlated FM order, and a second-order phase transition at $\Gamma = 0.75(5)$, which agrees relatively well with the results of Refs. [46,48,50]. More interestingly, for the LR-TQIM, the phase diagram hosts a LR-correlated columnar order, a LR-correlated clock $(0.5, -0.5, 0)$ order, a LR-correlated x-polarized FM order, and second-order phase transition lines in between. Notably, the detected clock order is different from the clock order found by recent mean-field/QMC results from Ref. [62]. Our numerical results argue for that in ladder-type highly-frustrated two-dimensional magnets: The LR quantum fluctuations always lead to LR correlations in the ground states. We expect our numerical claims to be justifiable in future ion-trap experiments and can be tested in forthcoming numerical simulations.

Our work raises several open questions regarding LR interactions in triangular lattices and provides some future research directions. Our results constitute the first simulation of such systems using iDMRG; however they are restricted to six-leg infinite cylinders. We have shown that $L_y = 6$ is large enough to provide higher than one-dimensional physical phenomena, while also being the smallest size that respects the tripartite symmetry and other requirements. Next research could investigate the phase diagram of the highly-frustrated H_{LR} on larger width cylinders to study the effect of the width on phase stabilization; this was successfully implemented for the SR-interacting J_1-J_2 triangular Heisenberg model [70] on YC8, 10, 12.

Working towards simulations on larger lattices is also important in the context of experimental quantum simulators based on trapped ions, which are achieving increasing numbers of spins in their simulation. The current state-of-the-art is 219 spins on a disk-shaped cluster [18] with physics that may more closely approximate the true 2D limit rather than the cylinder. The former is a limit that iDMRG simulations can describe more accurately as L_y increases.

The dynamics of such quantum simulators is also of interest, often more so than the static ground state properties. Time-dependent variation principle [80] and MPO-based [81] algorithms can be already used to time evolve an iMPS subjected to LR couplings; some progress in understanding the dynamics of the LR-TQIM on infinite cylinders has been already made by employing another MPO-based time-evolution approach [82]. Further developments of such algorithms may also open a path for finding finite-temperature states through the imaginary-time simulations.

Finally, our work highlights several foundational open questions of interest to both quantum information and condensed matter physicists. Is there a universal entanglement entropy scaling law for the LR-correlated phases in two dimensions? If there is, what are the corrections to the expected area law of entropy as found for the LR Hamiltonian in one dimension [42]? Similar to the significance of the area law of entropy for local gapped Hamiltonian, which provides the main reason behind the enormous success of MPS/DMRG for SR interactions, answering this question will assist in our collective attempt to fully classify LR-correlated quantum matter.

ACKNOWLEDGMENTS

The authors would like to thank Aroon O'Brien for discussions in the early stages of the project. S.N.S. and I.P.M. would also like to thank Tomohiro Hashizume for useful discussions and suggestions. This research was supported by the Australian Research Council (ARC) Centre of Excellence for Engineered Quantum Systems (EQuS), Project No. CE110001013, and by the ARC Centre of Excellence for Quantum Computation and Communication Technology (CQC2T), Project No. CE170100012. In addition, I.P.M. acknowledges the support from the ARC Future Fellowships scheme, FT140100625.

[1] U. Schollwöck, J. Richter, D. J. J. Farnell, and R. F. Bishop, editors, *Quantum Magnetism*, Vol. 645 of *Lecture Notes in Physics* (Springer, Berlin, Heidelberg, 2010).

[2] H. T. Diep, *Frustrated Spin Systems* (World Scientific, Singapore, 2004).

[3] C. Lhuillier, arXiv:cond-mat/0502464.

[4] C. Lacroix, P. Mendels, and F. Mila, *Introduction to Frustrated Magnetism: Materials, Experiments, Theory*, Springer Series in Solid-State Sciences (Springer, Berlin, Heidelberg, 2011).

[5] S. Sachdev, *Quantum Phase Transitions* (Cambridge University Press, New York, 2011).

[6] D. J. J. Farnell, O. Götze, J. Richter, R. F. Bishop, and P. H. Y. Li, Quantum $s = \frac{1}{2}$ antiferromagnets on archimedean lattices: The route from semiclassical magnetic order to nonmagnetic quantum states, Phys. Rev. B **89**, 184407 (2014).

[7] L. Néel, Propriétées magnétiques des ferrites; férrimagnétisme et antiferromagnétisme, Ann. Phys. (Paris) **3**, 137 (1948).

[8] X.-G. Wen, Quantum orders and symmetric spin liquids, Phys. Rev. B **65**, 165113 (2002).

[9] X. G. Wen, *Quantum Field Theory of Many-Body Systems: From the Origin of Sound to an Origin of Light and Electrons* (Oxford Graduate Texts, OUP Oxford, 2007).

[10] X. Chen, Z.-C. Gu, and X.-G. Wen, Local unitary transformation, long-range quantum entanglement, wave function renormalization, and topological order, Phys. Rev. B **82**, 155138 (2010).

[11] A. W. Sandvik, Ground States of a Frustrated Quantum Spin Chain with Long-Range Interactions, Phys. Rev. Lett. **104**, 137204 (2010).

[12] Z.-X. Gong, M. F. Maghrebi, A. Hu, M. L. Wall, M. Foss-Feig, and A. V. Gorshkov, Topological phases with long-range interactions, Phys. Rev. B **93**, 041102(R) (2016).

[13] Z.-X. Gong, M. F. Maghrebi, A. Hu, M. Foss-Feig, P. Richerme, C. Monroe, and A. V. Gorshkov, Kaleidoscope of quantum

phases in a long-range interacting spin-1 chain, Phys. Rev. B **93**, 205115 (2016).
[14] S. Fey and K. P. Schmidt, Critical behavior of quantum magnets with long-range interactions in the thermodynamic limit, Phys. Rev. B **94**, 075156 (2016).
[15] D. Jaschke, K. Maeda, J. D. Whalen, M. L. Wall, and L. D. Carr, Critical phenomena and Kibble-Zurek scaling in the long-range quantum Ising chain, New J. Phys. **19**, 033032 (2017).
[16] S. R. Manmana, M. Möller, R. Gezzi, and K. R. A. Hazzard, Correlations and enlarged superconducting phase of t-J chains of ultracold molecules on optical lattices, Phys. Rev. A **96**, 043618 (2017).
[17] J. W. Britton, B. C. Sawyer, A. C. Keith, C.-C. J. Wang, J. K. Freericks, H. Uys, M. J. Biercuk, and J. J. Bollinger, Engineered two-dimensional Ising interactions in a trapped-ion quantum simulator with hundreds of spins, Nature (London) **484**, 489 (2012).
[18] J. G. Bohnet, B. C. Sawyer, J. W. Britton, M. L. Wall, A. M. Rey, M. Foss-Feig, and J. J. Bollinger, Quantum spin dynamics and entanglement generation with hundreds of trapped ions, Science **352**, 1297 (2016).
[19] H. Labuhn, Creating arbitrary 2D arrays of single atoms for the simulation of spin systems with Rydberg states, H. Eur. Phys. J. Spec. Top. **225**, 2817 (2016).
[20] M. Gärttner, J. G. Bohnet, A. Safavi-Naini, M. L. Wall, J. J. Bollinger, and A. M. Rey, Measuring out-of-time-order correlations and multiple quantum spectra in a trapped-ion quantum magnet, Nat. Phys. **13**, 781 (2017).
[21] R. P. Feynman, Simulating physics with computers, Int. J. Theor Phys. **21**, 467 (1982).
[22] S. Lloyd, Universal quantum simulators, Science **273**, 1073 (1996).
[23] I. Buluta and F. Nori, Quantum simulators, Science **326**, 108 (2009).
[24] P. Hauke, F. M. Cucchietti, L. Tagliacozzo, I. Deutsch, and M. Lewenstein, Can one trust quantum simulators? Rep. Prog. Phys. **75**, 082401 (2012).
[25] I. Affleck, T. Kennedy, E. H. Lieb, and H. Tasaki, Rigorous Results on Valence-Bond Ground States in Antiferromagnets, Phys. Rev. Lett. **59**, 799 (1987).
[26] D. Perez-Garcia, F. Verstraete, M. M. Wolf, and J. I. Cirac, Matrix product state representations, Quantum Info. Comput. **7**, 401 (2007).
[27] I. P. McCulloch, From density-matrix renormalization group to matrix product states, J. Stat. Mech.: Theor. Exp. (2007) P10014.
[28] I. P. McCulloch, arXiv:0804.2509.
[29] L. Michel and I. P. McCulloch, arXiv:1008.4667.
[30] U. Schollwöck, The density-matrix renormalization group in the age of matrix product states, Ann. Phys. **326**, 96 (2011).
[31] R. Orus, A practical introduction to tensor networks: Matrix product states and projected entangled pair states, Ann. Phys. **349**, 117 (2014).
[32] S. R. White, Density Matrix Formulation for Quantum Renormalization Groups, Phys. Rev. Lett. **69**, 2863 (1992).
[33] S. R. White, Density-matrix algorithms for quantum renormalization groups, Phys. Rev. B **48**, 10345 (1993).
[34] M. F. Maghrebi, Z.-X. Gong, and A. V. Gorshkov, Continuous Symmetry Breaking in 1D Long-Range Interacting Quantum Systems, Phys. Rev. Lett. **119**, 023001 (2017).
[35] N. D. Mermin and H. Wagner, Absence of Ferromagnetism or Antiferromagnetism in One- or Two-Dimensional Isotropic Heisenberg Models, Phys. Rev. Lett. **17**, 1133 (1966).
[36] P. C. Hohenberg, Existence of long-range order in one and two dimensions, Phys. Rev. **158**, 383 (1967).
[37] D. Peter, S. Müller, S. Wessel, and H. P. Büchler, Anomalous Behavior of Spin Systems with Dipolar Interactions, Phys. Rev. Lett. **109**, 025303 (2012).
[38] A. Hamma, R. Ionicioiu, and P. Zanardi, Bipartite entanglement and entropic boundary law in lattice spin systems, Phys. Rev. A **71**, 022315 (2005).
[39] A. Hamma, R. Ionicioiu, and P. Zanardi, Ground state entanglement and geometric entropy in the kitaev model, Phys. Lett. A **337**, 22 (2005).
[40] A. Kitaev and J. Preskill, Topological Entanglement Entropy, Phys. Rev. Lett. **96**, 110404 (2006).
[41] M. Levin and X.-G. Wen, Detecting Topological Order in a Ground State Wave Function, Phys. Rev. Lett. **96**, 110405 (2006).
[42] T. Koffel, M. Lewenstein, and L. Tagliacozzo, Entanglement Entropy for the Long-Range Ising Chain in a Transverse Field, Phys. Rev. Lett. **109**, 267203 (2012).
[43] Z.-X. Gong, M. Foss-Feig, F. G. S. L. Brandao, and A. V. Gorshkov, Entanglement Area Laws for Long-Range Interacting Systems, Phys. Rev. Lett. **119**, 050501 (2017).
[44] J. Schachenmayer, B. P. Lanyon, C. F. Roos, and A. J. Daley, Entanglement Growth in Quench Dynamics with Variable Range Interactions, Phys. Rev. X **3**, 031015 (2013).
[45] D. Vodola, L. Lepori, E. Ercolessi, and G. Pupillo, Long-range Ising and Kitaev models: Phases, correlations and edge modes, New J. Phys. **18**, 015001 (2016).
[46] R. Moessner and S. L. Sondhi, Ising models of quantum frustration, Phys. Rev. B **63**, 224401 (2001).
[47] R. Moessner, S. L. Sondhi, and P. Chandra, Phase diagram of the hexagonal lattice quantum dimer model, Phys. Rev. B **64**, 144416, (2001).
[48] S. V. Isakov and R. Moessner, Interplay of quantum and thermal fluctuations in a frustrated magnet, Phys. Rev. B **68**, 104409 (2003).
[49] M. Powalski, K. Coester, R. Moessner, and K. P. Schmidt, Disorder by disorder and flat bands in the kagome transverse field Ising model, Phys. Rev. B **87**, 054404 (2013).
[50] K. A. Penson, R. Jullien, and P. Pfeuty, Triangular antiferromagnetic Ising model with a transverse field at zero temperature, J. Phys. C **12**, 3967 (1979).
[51] A. L. Burin, Many-body delocalization in a strongly disordered system with long-range interactions: Finite-size scaling, Phys. Rev. B **91**, 094202 (2015).
[52] F. Alet and N. Laflorencie, arXiv:1711.03145.
[53] J.-Y. Choi, S. Hild, J. Zeiher, P. Schauß, A. Rubio-Abadal, T. Yefsah, V. Khemani, D. A. Huse, I. Bloch, and C. Gross, Exploring the many-body localization transition in two dimensions, Science **352**, 1547 (2016).
[54] J. Smith, A. Lee, P. Richerme, B. Neyenhuis, P. W. Hess, P. Hauke, M. Heyl, D. A. Huse, and C. Monroe, Many-body localization in a quantum simulator with programmable random disorder, Nat. Phys. **12**, 907 (2016).
[55] K. Xu, J.-J. Chen, Y. Zeng, Yu-Ran Zhang, C. Song, W. Liu, Q. Guo, P. Zhang, Da Xu, H. Deng, K. Huang, H. Wang, X. Zhu, D. Zheng, and H. Fan, Emulating Many-Body Localization with

a Superconducting Quantum Processor, Phys. Rev. Lett. **120**, 050507 (2018).

[56] G. H. Wannier, Antiferromagnetism. The triangular ising net, Phys. Rev. **79**, 357 (1950).

[57] J. Stephenson, Ising model spin correlations on the triangular lattice. III. Isotropic antiferromagnetic lattice, J. Math. Phys. **11**, 413 (1970).

[58] M. Suzuki, Relationship between d-Dimensional Quantal Spin Systems and (d+1)-Dimensional Ising Systems: Equivalence, Critical Exponents and Systematic Approximants of the Partition Function and Spin Correlations, Prog. Theor. Phys. **56**, 1454 (1976).

[59] D. Blankschtein, M. Ma, A. N. Berker, G. S. Grest, and C. M. Soukoulis, Orderings of a stacked frustrated triangular system in three dimensions, Phys. Rev. B **29**, 5250(R) (1984).

[60] R. Moessner, S. L. Sondhi, and P. Chandra, Two-Dimensional Periodic Frustrated Ising Models in a Transverse Field, Phys. Rev. Lett. **84**, 4457 (2000).

[61] S. Alexander and P. Pincus, Phase transitions of some fully frustrated models, J. Phys. A: Math. Gen. **13**, 263 (1980).

[62] S. Humeniuk, Quantum Monte Carlo study of long-range transverse-field Ising models on the triangular lattice, Phys. Rev. B **93**, 104412 (2016).

[63] E. M. Stoudenmire and S. R. White, Quantum Monte Carlo study of long-range transverse-field Ising models on the triangular lattice, Annu. Rev. Condens. Matter Phys. **93**, 111 (2012).

[64] G. M. Crosswhite, A. C. Doherty, and G. Vidal, Applying matrix product operators to model systems with long-range interactions, Phys. Rev. B **78**, 035116 (2008).

[65] C. Hubig, I. P. McCulloch, and U. Schollwöck, Generic construction of efficient matrix product operators, Phys. Rev. B **95**, 035129 (2017).

[66] F. D. M. Haldane, Exact Jastrow-Gutzwiller Resonating-Valence-Bond Ground State of the Spin-(1/2 Antiferromagnetic Heisenberg Chain with $\frac{1}{r^2}$ Exchange, Phys. Rev. Lett. **60**, 635 (1988).

[67] B. Sriram Shastry, Exact Solution of an S=1/2 Heisenberg Antiferromagnetic Chain with Long-Ranged Interactions, Phys. Rev. Lett. **60**, 639 (1988).

[68] G. H. Golub and C. F. Van Loan, *Matrix Computations* (Johns Hopkins University Press, Baltimore, 2012).

[69] S. N. Saadatmand, Frustrated spin systems, an MPS approach. Ph.D. thesis, The University of Queensland, Australia, 2017.

[70] S. N. Saadatmand and I. P. McCulloch, Detection and characterization of symmetry-broken long-range orders in the spin-$\frac{1}{2}$ triangular Heisenberg model, Phys. Rev. B **96**, 075117 (2017).

[71] S. Östlund and S. Rommer, Thermodynamic Limit of Density Matrix Renormalization, Phys. Rev. Lett. **75**, 3537 (1995).

[72] S. Rommer and S. Östlund, Class of ansatz wave functions for one-dimensional spin systems and their relation to the density matrix renormalization group, Phys. Rev. B **55**, 2164 (1997).

[73] I. Homrighausen, N. O. Abeling, V. Zauner-Stauber, and J. C. Halimeh, Anomalous dynamical phase in quantum spin chains with long-range interactions, Phys. Rev. B **96**, 104436 (2017).

[74] J. W. G. Wilder, L. C. Venema, A. G. Rinzler, R. E. Smalley, and C. Dekker, Electronic structure of atomically resolved carbon nanotubes, Nature (London) **391**, 59 (1998).

[75] S. R. White and A. L. Chernyshev, Neél Order in Square and Triangular Lattice Heisenberg Models, Phys. Rev. Lett. **99**, 127004 (2007).

[76] P. Lecheminant, B. Bernu, C. Lhuillier, and L. Pierre, J_1-J_2 quantum Heisenberg antiferromagnet on the triangular lattice: A group-symmetry analysis of order by disorder, Phys. Rev. B **52**, 6647 (1995).

[77] Z. Zhu and S. R. White, Spin liquid phase of the $s = \frac{1}{2} J_1 - J_2$ Heisenberg model on the triangular lattice, Phys. Rev. B **92**, 041105 (2015).

[78] W.-J. Hu, S.-S. Gong, W. Zhu, and D. N. Sheng, Competing spin-liquid states in the spin-$\frac{1}{2}$ Heisenberg model on the triangular lattice, Phys. Rev. B **92**, 140403(R) (2015).

[79] S. N. Saadatmand, B. J. Powell, and I. P. McCulloch, Phase diagram of the spin $-\frac{1}{2}$ triangular $J_1 - J_2$ Heisenberg model on a three-leg cylinder, Phys. Rev. B **91**, 245119 (2015).

[80] J. Haegeman, J. Ignacio Cirac, T. J. Osborne, I. Piorn, H. Verschelde, and F. Verstraete, Time-Dependent Variational Principle for Quantum Lattices, Phys. Rev. Lett. **107**, 070601 (2011).

[81] M. P. Zaletel, R. S. K. Mong, C. Karrasch, J. E. Moore, and F. Pollmann, Time-evolving a matrix product state with long-ranged interactions, Phys. Rev. B **91**, 165112 (2015).

[82] T. Hashizume and I. P. McCulloch (unpublished).